

Evolution and star formation history of NGC 300 from a chemical evolution model with radial gas inflows

Xiaoyu Kang^{1,2,3}, Rolf-Peter Kudritzki^{4,5}, Xiaobo Gong⁶, and Fenghui Zhang^{1,2,3}

¹ Yunnan Observatories, Chinese Academy of Sciences, 396 Yangfangwang, Guandu District, Kunming, 650216, P.R. China
e-mail: kxyysl@ynao.ac.cn

² Key Laboratory for the Structure and Evolution of Celestial Objects, Chinese Academy of Sciences, 396 Yangfangwang, Guandu District, Kunming, 650216, P. R. China

³ International Centre of Supernovae, Yunnan Key Laboratory, Kunming 650216, P. R. China

⁴ University Observatory Munich, Ludwig-Maximilian-Universität München, Scheinerstr. 1, 81679 Munich, Germany

⁵ Institute for Astronomy, University of Hawaii, 2680 Woodlawn Drive, Honolulu, HI96822, USA

⁶ School of Opto-electronic Engineering, Zaozhuang University, Zaozhuang, 277160, P.R. China

Received February 18, 2025; accepted July 14, 2025

ABSTRACT

Context. The cosmic time evolution of the radial structure is one of the key topics in the investigation of disc galaxies. In the build-up of galactic discs gas infall is an important ingredient and it produces radial gas inflows as a physical consequence of angular momentum conservation, since the infalling gas on to the disc at a specific radius has lower angular momentum than the circular motions of the gas at the point of impact. NGC 300 is a well studied isolated, bulge-less, and low-mass disc galaxy ideally suited for an investigation of galaxy evolution with radial gas inflows.

Aims. Our aim is to investigate the effects of radial gas inflows on the physical properties of NGC 300, such as, the radial profiles of H I gas mass and star formation rate (SFR) surface densities, specific star formation rate (sSFR) and metallicity, as well as to study how the metallicity gradient evolves with cosmic time.

Methods. A chemical evolution model for NGC 300 is constructed by assuming its disc builds up progressively by infalling of metal-free gas and outflowing of metal-enriched gas. Radial gas inflows are also considered in the model. We use the model to build a bridge between the available data (such as gas content, SFR, and chemical abundances) observed today and the galactic key physical processes.

Results. Our model including the radial gas inflows and an inside-out disc formation scenario can simultaneously reproduce the present-day observed radial profiles of H I gas mass surface density, SFR surface density, sSFR, gas-phase and stellar metallicity. We find that, although the value of radial gas inflow velocity is as low as -0.1 km s^{-1} , the radial gas inflows steepen the present-day radial profiles of H I gas mass surface density, SFR surface density, and metallicity, but flatten the radial sSFR profile. Incorporating radial gas inflows significantly improves the agreement between our model predicted present-day sSFR profile and the observations of NGC 300. Our model predictions are also in good agreement with the star-forming galaxy main sequence and the mass-metallicity relation of star-forming galaxies. It predicts a significant flattening of the metallicity gradient with cosmic time. We also find that the model predicted star formation has been more active recently, indicating that the radial gas inflows may be help to sustain star formation in local spirals, at least in NGC 300.

Key words. galaxies: evolution – galaxies: abundances: individual(NGC 300) – galaxies: spiral

1. Introduction

Metallicity acts as a fossil records of evolution and star formation history (SFH) of galaxies, because it plays a key role in many fundamental galactic physical processes, such as gas infall, star formation, stellar evolution, gas outflows. Metallicity can also provide clues on some additional physical processes in galaxies, including stellar migration and radial gas inflows within galactic discs. The complex interplay between the aforementioned physical processes that enhance metal production and those that reduce metals in galaxies provides important insights on the formation and assembly history of galaxies (Sánchez Almeida et al. 2014).

The study of the metallicity in a galaxy provides an essential test bed to explore its disc formation scenario and mass assembly history. In particular, spiral galaxies in the local Universe universally exhibit negative radial metallicity gradients, with inner re-

gions more metal enriched with respect to the outskirts of galactic discs (for example, Zaritsky et al. 1994; Magrini et al. 2009; Moustakas et al. 2010; Stasińska et al. 2013; Stanghellini et al. 2014; Pilyugin et al. 2014; Gazak et al. 2015; Zinchenko et al. 2019; Liu et al. 2022; Bresolin et al. 2022; Chen et al. 2023; Kudritzki et al. 2024; Sextl et al. 2024). Although negative radial metallicity gradients are common in the local Universe, there is no general consensus yet about the behaviour of metallicity gradients cosmic evolution: How are the present-day radial metallicity gradients established? Do they steepen, flatten, or remain fixed with time? In addition, the radial metallicity gradients and their temporal evolution encode the scenarios of disc formation, reflect the presence of gas infall and outflows, as well as radial gas inflows along the disc, and reveal the migration of stars.

Chemical evolution models, which can build a bridge between the chemical abundance patterns observed today and the

galactic key physical processes, are able to infer the SFH of spiral galaxies and the cosmic time evolution of their metallicity gradients. In this framework, the closed-box chemical evolution model (Schmidt 1963) failed to explain the relative paucity of observed low-metallicity stars (G-dwarf problem) in the solar neighbourhood (e.g., van den Bergh 1962; Haywood et al. 2019), indicating a necessity for inclusion of continuous gas infall in the chemical evolution model (Larson 1972; Dalcanton et al. 2004). To reproduce the observed radial metallicity gradients of galactic discs, an "inside-out" disc formation scenario, that is, inner regions of disc are formed earlier and on a shorter time-scales, has been applied in the model and supported by many works (e.g., Larson 1976; Matteucci & Francois 1989; Chiappini et al. 2001; Belfiore et al. 2019; Vincenzo & Kobayashi 2020; Grisoni et al. 2018; Frankel et al. 2019; Spitoni et al. 2021a). Low-mass galaxies are more efficient in losing metal-enriched matter than high-mass systems because the former have shallower gravitational potential wells (Kauffmann et al. 1993). Thus, the gas outflow process has become a ubiquitous component of galaxy evolution models (e.g., Larson 1974; Tremonti et al. 2004; Chang et al. 2010; Lian et al. 2018a; Spitoni et al. 2021b; Yin et al. 2023).

In addition, the radial motions of gas and star need to be considered in the chemical evolution model. While extremely difficult to be observed directly, radial gas flows are postulated on physical grounds (Lacey & Fall 1985). There are several mechanisms that could drive such gas flows: i) viscosity of the gaseous layer of the disc (Thon & Meusinger 1998), ii) gravitational interactions between the gas and the presence of the bars or spiral density waves in the disc (Kubryk et al. 2015), and iii) mismatch of the angular momentum between the infalling gas and the circular motions of the gas in the disc (e.g., Portinari & Chiosi 2000; Spitoni & Matteucci 2011; Grisoni et al. 2018; Vincenzo & Kobayashi 2020; Calura et al. 2023).

Radial migration of stars from their birth place to another galaxy region can also affect the metallicity gradients. The observed age-metallicity relationship in the solar neighbourhood of our Galaxy puts strong evidence on the presence of radial migration (e.g. Edvardsson et al. 1993; Haywood 2008; Schönrich & Binney 2009; Feuillet et al. 2019; Xiang & Rix 2022; Lian et al. 2022). In addition, theoretical and numerical studies suggest that radial stellar migration can be boosted by several process such as mergers or interactions with satellites (Quillen et al. 2009; Bird et al. 2012; Carr et al. 2022), the presence of transient spiral structures (Sellwood & Binney 2002; Roškar et al. 2008; Daniel & Wyse 2015; Loebman et al. 2016), as well as the central bars (Minchev & Famaey 2010; Kubryk et al. 2013; Halle et al. 2015; Khoperskov et al. 2020).

The nearby flocculent low-mass spiral galaxy NGC 300 is a perfect target for studying the secular star formation histories and galactic evolution. With a distance of $d = 2$ Mpc (Dalcanton et al. 2009, but see also Gieren et al. 2005 and Sefton et al. 2021 for slightly different distances), it is the closest nearly face-on and isolated (Karachentsev et al. 2003), star-forming (Kruijssen et al. 2019) and bulge-less (Vlajić et al. 2009; Williams et al. 2013) disc galaxy with well observed radial profiles of gas mass, star mass, and star formation rate (SFR) surface densities. We will use a chemical evolution model with gas infall and outflows to match the observations.

This paper is structured as follows. Section 2 presents the main ingredients of the chemical evolution model used in this work. Section 3 presents the main observed data of the target

galaxy used to constrain the model. Section 4 presents our results. Sect. 5 gives conclusions.

2. Model

The chemical evolution model adopted in this work is based on Kang et al. (2016). The NGC 300 disc is assumed to progressively build up by infalling of primordial gas ($X = 0.7571$, $Y_p = 0.2429$, $Z = 0$) from its halo and outflowing of metal-enriched gas, and it is composed of a number of concentric rings. The main improvement of the model is the implementation of radial inflows of gas following the prescriptions described in Portinari & Chiosi (2000) and Spitoni & Matteucci (2011). Radial stellar migration is not considered in the model, since the kinematics of globular cluster systems (Olsen et al. 2004; Nantais et al. 2010), N-body simulations studies (Gogarten et al. 2010), and the lack of a radial age inversion (Gogarten et al. 2010), as well as a pure exponential disc (Bland-Hawthorn et al. 2005) and the weak transient structure (Cohen et al. 2024) all together indicate that NGC 300 has not undergone significant radial stellar migrations during its evolution.

Main ingredients of the model are the inclusion of infalls of metal-poor gas, star formation law, outflows of metal-enriched gas and radial gas inflows. The instantaneous recycling approximation (IRA) is adopted in the model by assuming that stars more massive than $1M_\odot$ die instantaneously, while those stars less than $1M_\odot$ live forever. The enriched gas is ejected and rapidly becomes well-mixed with the surrounding interstellar medium (ISM). IRA is an acceptable approximation for chemical elements produced by massive stars with short lifetimes, such as oxygen. On the other hand, IRA is a poor approximation for chemical elements produced by stars with long lifetimes, such as nitrogen, carbon and iron (see Vincenzo et al. 2016; Matteucci 2021). Oxygen is most abundant heavy element by mass in the universe, and it is the best proxy for the global metallicity of the galaxy ISM. Thus, oxygen abundance (i.e. $12 + \log(\text{O}/\text{H})$) will be used to represent the metallicity of NGC 300 throughout this work. The details of the set of equations and main ingredients of the model are as follows.

2.1. Equations of chemical evolution

We assume azimuthal homogeneity. The evolution in each ring at galactocentric radius r during time t can be described by three differential equations. The first one relates the change of the total mass (stars and gas) surface density $\Sigma_{\text{tot}}(r, t)$ to the rates of gas infall $f_{\text{in}}(r, t)$ and outflow $f_{\text{out}}(r, t)$ at the corresponding radius and time, respectively

$$\frac{d[\Sigma_{\text{tot}}(r, t)]}{dt} = f_{\text{in}}(r, t) - f_{\text{out}}(r, t), \quad (1)$$

The evolution of the gas mass surface density $\Sigma_{\text{gas}}(r, t)$ is described in the second equation through

$$\frac{d[\Sigma_{\text{gas}}(r, t)]}{dt} = -(1-R)\Psi(r, t) + f_{\text{in}}(r, t) - f_{\text{out}}(r, t) + \left[\frac{d\Sigma_{\text{gas}}(r, t)}{dt}\right]_{rf}, \quad (2)$$

where $\Psi(r, t)$ the SFR surface density at the corresponding place and time. R is the fraction of stellar mass returned to the ISM. The last term in the equation $\left[\frac{d\Sigma_{\text{gas}}(r, t)}{dt}\right]_{rf}$ accounts for the change of gas mass surface density through the radial gas flows and will be described below.

The third differential equation considers the evolution of metallicity $Z(r, t)$ as the result of star formation and nucleosynthesis. It also accounts for the effects of radial flows through the term $[\frac{d[Z(r, t)\Sigma_{\text{gas}}(r, t)]}{dt}]_{rf}$, which will also be described below

$$\begin{aligned} \frac{d[Z(r, t)\Sigma_{\text{gas}}(r, t)]}{dt} = & y(1 - R)\Psi(r, t) - Z(r, t)(1 - R)\Psi(r, t) \\ & + Z_{\text{in}}f_{\text{in}}(r, t) - Z_{\text{out}}(r, t)f_{\text{out}}(r, t) \\ & + [\frac{d[Z(r, t)\Sigma_{\text{gas}}(r, t)]}{dt}]_{rf}, \end{aligned} \quad (3)$$

where y is the nuclear metal synthesis yield.

For the values of R and y , we adopt $R = 0.289$ and $y = 0.0099$, which are averages over metallicity obtained from Table 2 of Vincenzo et al. (2016) (see also Romano et al. 2010) for the initial mass function (IMF) of Kroupa et al. (1993). The dependence on metallicity and time is weak and, thus, we work with constant average values. On the other hand, the chemical enrichment of galaxies depends largely on the IMF (Vincenzo et al. 2016; Goswami et al. 2021) and the Kroupa IMF is the preferred describing the chemical evolution of spiral discs as pointed out in the references just given.

Z_{in} is the metallicity of the infalling gas. In this work, Z_{in} is assumed to be a function of time to approximate the recycling effects caused by mixing of the infalling gas from intergalactic medium (IGM) with gas outflows in the circumgalactic medium (CGM) of NGC 300, after which gas is recycled back into the disc. Kang et al. (2023) found that most of the stellar mass of M33-mass bulgeless spiral galaxies were assembled at $z < 1$. As a result, Z_{in} is assumed to be primordial ($Z_{\text{in}} = 0$) at redshift $z > 0.7$. For $z \leq 0.7$, we model its metallicity as a time dependent function to approximate the recycling effect, i.e., $Z_{\text{in}}/Z_{\odot} = k \times t + b$, where t represents the evolutionary time in units of Gyr, and the age of the universe at $z = 0$ is 13.5 Gyr. The slope of the time-dependent metallicity function (k) for the infalling gas is determined by referencing the metallicity evolution trend in the NGC 300 disc, as shown in the lower-right panel of Figure 8 of Kang et al. (2016). The Z_{in}/Z_{\odot} -intercept (b) is obtained from the metallicity of CGM at the present day, which spans $-1.0 < \log(Z/Z_{\odot}) < -0.5$ (Prochaska et al. 2017; Pointon et al. 2019). As for NGC 300, the present-day metallicity of CGM is assumed to be -0.75 . Therefore, the functional form of metallicity of the infalling gas is given by $Z_{\text{in}}/Z_{\odot} = 0.039 \times t - 0.348$.

$Z_{\text{out}}(r, t)$ is the metallicity of the outflowing gas, and its value is assumed to be identical to that of ISM at the time the outflows are launched, i.e. $Z_{\text{out}}(r, t) = Z(r, t)$ (Ho et al. 2015; Kudritzki et al. 2015).

2.2. Main ingredients

Continuous infall of primordial gas is invoked in the chemical evolution model to explain the relative scarcity of observed low-metallicity stars (G-dwarf problem) in galaxy discs (e.g., van den Bergh 1962; Haywood et al. 2019). The primordial gas infall rate at each radius r and time t , $f_{\text{in}}(r, t)$, in units of $\text{M}_{\odot} \text{pc}^{-2} \text{Gyr}^{-1}$, is expressed by:

$$f_{\text{in}}(r, t) = A(r) \cdot t \cdot e^{-t/\tau}, \quad (4)$$

where τ is the gas infall timescale. Following Matteucci & Franco (1989) and Kang et al. (2016), the infall timescale has the form $\tau(r) = a \times r/R_d + b$. In this way, it takes the gas longer to settle onto the disc in the outer regions, corresponding to a scenario inside-out disc formation. $R_d = 1.29 \text{ kpc}$ is the present-day disc scale-length and

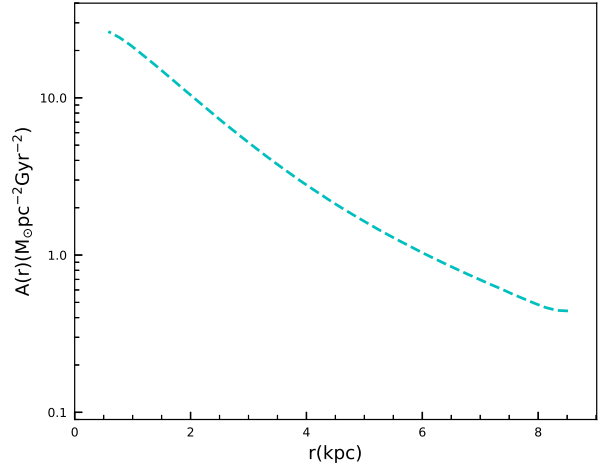


Fig. 1. The function $A(r)$ obtained with the best-fitting model of NGC 300 (see Section 4).

derived from the observed K -band luminosity distribution (Muñoz-Mateos et al. 2007) together with a total stellar mass of $M_* = 1.928 \times 10^9 \text{ M}_{\odot}$ (Muñoz-Mateos et al. 2007). The coefficients a and b for $\tau(r)$ are free parameters in our model and will be determined below.

While a simple exponential form of gas infall rate is a popular assumption in many previous chemical evolution models (e.g., Matteucci & Franco 1989; Yin et al. 2009; Spitoni et al. 2020; Calura et al. 2023), the gas infall rate form adopted in this work includes more possible scenarios and is more suitable for low-mass galaxies. The reader is referred to Kang et al. (2016) for a more indepth descriptions of the difference between these two gas infall forms.

The function $A(r)$ modifies the infall rate as a function of galactocentric radius and is iteratively constrained by requesting that the present-day model stellar mass surface density $\Sigma_*(r, t_g)$ follows the observed exponential profile:

$$\Sigma_*(r, t_g) = \Sigma_*(0, t_g) \exp(-r/R_d), \quad (5)$$

$\Sigma_*(0, t_g)$ is the present-day central stellar mass surface density, and it can be obtained from $\Sigma_*(0, t_g) = M_*/2\pi R_d^2$. t_g is the cosmic age and with $t_g = 13.5 \text{ Gyr}$ according to the standard flat cosmology.

In our calculation, after fixing the values of τ , we start with an initial distribution of $A(r)$ and numerically solve the gas evolution (Eq. 2) and the increase of stellar mass (via Eq. 1) adopting a SFR surface density $\Psi(r, t)$ (see below). By comparing the resulted $\Sigma_*(r, t_g)$ with its observed value, we adjust the value of $A(r)$ and repeat the calculation until the resulting $\Sigma_*(r, t_g)$ agrees well with the observed radial distribution. Figure 1 plots the best-fitting model (see Section 4) predicted radial profile of $A(r)$.

The SFR surface density $\Psi(r, t)$ (in units of $\text{M}_{\odot} \text{pc}^{-2} \text{Gyr}^{-1}$) describes the amount cold gas turning into stars per unit time. Following Leroy et al. (2008), Krumholz (2014) and Kang et al. (2016, 2023), we adopt $\Psi(r, t)$ proportional to the molecular gas mass surface density $\Sigma_{\text{H}_2}(r, t)$

$$\Psi(r, t) = \Sigma_{\text{H}_2}(r, t)/t_{\text{dep}}, \quad (6)$$

t_{dep} is the molecular gas depletion time, and its value is taken as $t_{\text{dep}} = 1.9 \text{ Gyr}$ (Leroy et al. 2008). In order to calculate $\Sigma_{\text{H}_2}(r, t)$, we need to split the total gas mass surface density into its atomic

and molecular components. This is done in the same way as described in detail in [Kang et al. \(2023\)](#).

NGC 300 is a low-mass disc galaxy with shallow gravitational potential and a low rotation speed, making it efficient in expelling metal-enriched matter ([Tremonti et al. 2004](#); [Hirschmann et al. 2016](#); [Lian et al. 2018a](#); [Spitoni et al. 2020](#)). The gas outflow rate $\dot{f}_{\text{out}}(r, t)$ (in units of $M_{\odot} \text{pc}^{-2} \text{Gyr}^{-1}$) is assumed to be proportional to $\Psi(r, t)$ (see [Recchi et al. 2008](#)):

$$\dot{f}_{\text{out}}(r, t) = b_{\text{out}} \Psi(r, t), \quad (7)$$

where b_{out} is the gas outflow efficiency (dimensionless quantity), and it is also a free parameter in the model. We emphasize that the outflow efficiency is assumed to be constant, since the outflow process is energetically driven by star formation, and b_{out} simply reflects the efficiency of energy transfer from star formation to the gas outflow.

2.3. Implementation of radial inflows

The groundbreaking works of [Tinsley & Larson \(1978\)](#) and [Mayor & Vigroux \(1981\)](#) highlight the potential importance of radial gas flows for the chemical evolution of galactic discs. Radial gas flows are the physical consequence of the gas infall, because the specific angular momentum of the infalling gas is lower than the gas circular motions in the disc, and mixing between the two will induce a net radial gas inflow. In consequence, they should be considered if one assumes that the galactic disc is formed by gas infall. We implement the radial gas inflows in our chemical evolution model based on the prescriptions and formalism of [Portinari & Chiosi \(2000\)](#) and [Spitoni & Matteucci \(2011\)](#). Following [Spitoni et al. \(2013\)](#) and [Grisoni et al. \(2018\)](#) the radial inflow velocity is assumed to be related to the galactocentric distance, i.e., $|v_R| = c \times r/R_d + d$, where c and d are the coefficients for v_R .

In our numerical solution of equations (1) to (3) we divide the galactic disc into discrete shells. The k -th shell has the galactocentric radius r_k and inner and outer edges named as $r_{k-\frac{1}{2}}$ and $r_{k+\frac{1}{2}}$, respectively. Through these edges, gas inflow can occur with velocities $v_{k-\frac{1}{2}}$ and $v_{k+\frac{1}{2}}$, respectively. The gas flow velocities are taken positive outwards and negative inwards.

Radial inflows through the edges, with a flux $F(r)$, alter the gas mass surface density $\Sigma_{\text{gas}}(r_k)$ in the k -th shell according to:

$$\left[\frac{d\Sigma_{\text{gas}}(r_k)}{dt} \right]_{rf} = - \frac{1}{\pi(r_{k+\frac{1}{2}}^2 - r_{k-\frac{1}{2}}^2)} [F(r_{k+\frac{1}{2}}) - F(r_{k-\frac{1}{2}})], \quad (8)$$

where the gas flow at $r_{k-\frac{1}{2}}$ and $r_{k+\frac{1}{2}}$ can be written as

$$F(r_{k-\frac{1}{2}}) = 2\pi r_{k-\frac{1}{2}} v_{k-\frac{1}{2}} [\Sigma_{\text{gas}}(r_{k-1})], \quad (9)$$

and

$$F(r_{k+\frac{1}{2}}) = 2\pi r_{k+\frac{1}{2}} v_{k+\frac{1}{2}} [\Sigma_{\text{gas}}(r_{k+1})], \quad (10)$$

The inner edge of k -th shell, $r_{k-\frac{1}{2}}$, is taken at the mid-point between the characteristic radii of the shells k -th and $k-1$ -th,

$$r_{k-\frac{1}{2}} = (r_{k-1} + r_k)/2, \quad (11)$$

and similarly for the outer edge $r_{k+\frac{1}{2}}$

$$r_{k+\frac{1}{2}} = (r_k + r_{k+1})/2, \quad (12)$$

From Eqs. 11 and 12, we can obtain that

$$(r_{k+\frac{1}{2}}^2 - r_{k-\frac{1}{2}}^2) = \frac{r_{k+1} - r_{k-1}}{2} (r_k + \frac{r_{k-1} + r_{k+1}}{2}), \quad (13)$$

Combining Eqs. 8, 9, 10, and 13 and, we can get radial flow term $\left[\frac{d[Z(r_k, t) \Sigma_{\text{gas}}(r_k, t)]}{dt} \right]_{rf}$ of Eq. 3 as follows:

$$\left[\frac{d[Z(r_k, t) \Sigma_{\text{gas}}(r_k, t)]}{dt} \right]_{rf} = -\beta_k Z(r_k, t) \Sigma_{\text{gas}}(r_k, t) + \gamma_k Z(r_{k+1}, t) \Sigma_{\text{gas}}(r_{k+1}, t), \quad (14)$$

where

$$\beta_k = - \frac{2}{r_k + \frac{r_{k-1} + r_{k+1}}{2}} \times [v_{k-\frac{1}{2}} \frac{r_{k-1} + r_k}{r_{k+1} - r_{k-1}}], \quad (15)$$

and

$$\gamma_k = - \frac{2}{r_k + \frac{r_{k-1} + r_{k+1}}{2}} \times [v_{k+\frac{1}{2}} \frac{r_k + r_{k+1}}{r_{k+1} - r_{k-1}}]. \quad (16)$$

In summary, we note that our model has five free parameters (a , b , c , d , and b_{out}). The first two - a and b - characterize the gas infall time scale τ , the next two - c and d - describe the radial gas flow within the disc, and the fifth parameter b_{out} constrains the gas outflow efficiency. The determination of the best combination of these parameters will be described in Sect. 4.

3. Observations

The major goal of our chemical evolution model is to use the stellar and gas content, SFR, and chemical abundances observed today to infer the galaxy star formation history (SFH) and how the chemical composition and metallicity gradients evolve with cosmic time. The details of the available observations used to constrain the model are described in the following.

The atomic hydrogen (H I) gas of NGC 300 is obtained from the Australia Telescope Compact Array (ATCA), and the radial profile of the H I mass surface density (Σ_{HI}) of NGC 300 is taken from [Westmeier et al. \(2011\)](#). As already mentioned above, the stellar mass of the NGC 300 disc is obtained from the K -band luminosity. The value is $M_* \sim 1.928 \times 10^9 M_{\odot}$ ([Muñoz-Mateos et al. 2007](#)).

The radial profiles of SFR surface density (Σ_{SFR}) of NGC 300 is determined from Hubble Space Telescope (HST) resolved stellar populations ([Gogarten et al. 2010](#)), the combination of far-ultraviolet (FUV) and 24 μm maps ([Williams et al. 2013](#)), and the FUV image ([Mondal et al. 2019](#)). The current total SFR in the disc of NGC 300 is reported to be in the range $\sim 0.08 - 0.46 M_{\odot} \text{yr}^{-1}$ using different tracers, such as the X-ray luminosity ([Binder et al. 2012](#)), FUV luminosity ([Karachentsev & Kaisina 2013](#); [Mondal et al. 2019](#)), H α emission ([Helou et al. 2004](#); [Karachentsev & Kaisina 2013](#); [Kruijssen et al. 2019](#)), mid-infrared (MIR, [Helou et al. 2004](#)), the HST resolved stars ([Gogarten et al. 2010](#)) and the spectral energy distribution (SED) modeling ([Casasola et al. 2022](#); [Binder et al. 2024](#)).

The specific SFR (sSFR) is defined as SFR per unit of stellar mass. The observed sSFR value for NGC 300 can be computed from $\text{sSFR} = \frac{\text{SFR}}{M_*}$, i.e., $-10.382 \leq \log(\text{sSFR}/\text{yr}^{-1}) \leq -9.622$. The radial profile of sSFR has been derived by [Muñoz-Mateos et al. \(2007\)](#), who used the (FUV- K) color profile of NGC 300 and adopted a proper SFR calibration of the FUV luminosity and K -band mass-to-light ration.

Crucial additional constraints on the evolution of NGC 300 are obtained from the radial distribution of metallicity. Contrary to our previous work (Kang et al. 2016, 2023), we additionally rely on accurate metallicity measurements based on detailed non-LTE spectroscopy of very young massive stars, blue supergiants (BSGs, Kudritzki et al. 2008) and red supergiants (RSGs, Gazak et al. 2015). (Note that we have applied the relationship in the appendix of Davies et al. 2017 to put the RSG on the same metallicity scale as the BSG). We convert the metallicities of these very young stars to oxygen abundances via $12 + \log(\text{O}/\text{H}) = \log Z/Z_{\odot} + 8.69$ using the solar oxygen abundance (Asplund et al. 2009). We then also use the H α regions oxygen abundances obtained by Bresolin et al. (2009), which are based on the analysis of collisionally excited lines and the T_e method. In addition, we also compare with oxygen abundances of planetary nebulae (PNe) (Stasińska et al. 2013), which represent metallicities at intermediate ages.

4. Results and discussion

The collection of observed data displayed in Figure 2 is used to constrain our model and its five free parameters (see Sect. 2). We firstly computed the radial profiles of H α mass and SFR surface density, sSFR, and $12 + \log(\text{O}/\text{H})$ along the disc of NGC 300 and compare them to available observed data to search for the best-fitting model for NGC 300. Note that the $12 + \log(\text{O}/\text{H})$ data are all together combined into the 12 radial bins displayed in Fig. 8.

As in Kang et al. (2016), the classical χ^2 technique is adopted to calculate the best combination of free parameters, which we vary within the range of $0 < a \leq 3.0$, $1.0 \leq b \leq 5.0$, $0.1 \leq 0 \leq c \times r/R_d + d \leq 1.0$, and $0 < b_{\text{out}} \leq 1.0$. We obtain $(a, b, c, d, b_{\text{out}}) = (0.16, 3.0, 0.0, 0.1, 0.6)$, i.e., $(\tau, v_R, b_{\text{out}}) = (0.16r/R_d + 3.0 \text{ Gyr}, -0.1 \text{ km s}^{-1}, 0.6)$. The model calculated with these parameters is called Model B. The results corresponding to Model B are plotted by solid lines in Fig. 2. A remarkable agreement is found between the Model B predictions and the NGC 300 observations, that is, the Model B results can simultaneously reproduce the radial observed profiles of H α gas mass surface density, SFR surface density, sSFR and $12 + \log(\text{O}/\text{H})$.

The best-fitting model of NGC 300 without radial gas inflows in Kang et al. (2016) (“Model A”) with parameters $(\tau, v_R, b_{\text{out}}) = (0.52r/R_d + 2.6 \text{ Gyr}, 0, 0.9)$ is also plotted as in Fig. 2 as a dashed line. We see that Model A is also basically able to reproduce the observed data. The differences between the two models are small, but there are clear systematic trends. The radial gas inflows steepen the present-day radial profiles of H α gas mass surface density, SFR surface density, and metallicity, but flatten the radial sSFR profile. The steeper profiles of gas mass surface density and metallicity predicted by Model B are consistent with the result of Calura et al. (2023). We also note that the central increase in metallicity of Model B is in better agreement with the observations.

$v_R = -0.1 \text{ km s}^{-1}$ appears to be a very small value. However, it is supported by a study of 54 local spiral galaxies based on high-sensitive and high-resolution data of the H α emission line, which finds that the radial inflow velocities are generally small, with an average inflow rate of about -0.3 km s^{-1} (Di Teodoro & Peek 2021).

The left panel of Fig. 3 shows that, compared to Model A, Model B predicts both delayed and more extended star formation. The peak of SFR from Model B is shifted by 1 Gyr. The SFR predicted by Model B and Model A are respectively $\sim 0.16 M_{\odot} \text{ yr}^{-1}$ and $\sim 0.15 M_{\odot} \text{ yr}^{-1}$, consistent with the observed values (see Section 3). The right panel of Fig. 3 shows that,

both Model A and Model B predicted galaxy stellar masses have been steadily increasing to their present-day values. Compared to Model A, Model B forms stars later. The right panel agrees well with the bottom panel of Fig 17 in Sextl et al. (2023), which based on the galaxy evolution model of Kudritzki et al. (2021) led to the conclusion that most of galaxy stellar masses has been assembled in the last 10 Gyr. Fig. 3 indicates that the radial gas inflows help to sustain star formation in local spirals, at least in NGC 300.

An additional test of our model is obtained by a comparison with the observed mean metallicities for the entire stellar population as derived from the photometric analysis of color-magnitude diagrams (CMD) in Gogarten et al. (2010). The comparison is carried out in Fig. 4. The model mass-weighted average stellar metallicity at galactocentric radius r and time t is calculated as (Pagel 1997; Kang et al. 2021)

$$\langle Z_{\text{star}}(r, t_g) \rangle = \frac{\int_0^{t_g} Z_{\text{gas}}(r, t') \text{SFR}(r, t') dt'}{\int_0^{t_g} \text{SFR}(r, t') dt'}. \quad (17)$$

Given the uncertainties of the purely photometric diagnostics the agreement is quite compelling. We note the Model B predicted metallicity average over all different stellar ages is about $\sim 0.2 \text{ dex}$ smaller than the one of the present-day ISM and the very young stellar population. This agrees with cosmological simulations and corresponding chemical evolution models (Finlator & Davé 2008; Pipino et al. 2014; Peng & Maiolino 2014, etc.) and the observational work (e.g., Halliday et al. 2008; Fraser-McKelvie et al. 2022). Based on analyzing the integrated stellar population absorption line spectra of $\sim 200,000$ star-forming galaxies in the Sloan Digital Sky Survey, Sextl et al. (2023) also derived that, for a galaxy with stellar mass $(\log(M_*/M_{\odot}) \sim 9.3)$, the metallicity difference between the young stellar population and average metallicity is about $\sim 0.2 \text{ dex}$. In addition, we find that the Model B predicted stellar metallicity gradient exhibits a steeper slope compared to the gas-phase gradient, which aligns with previous statistical findings from observational studies (Lian et al. 2018b; Sánchez-Blázquez 2020, and reference therein).

An additional important test of our galaxy evolution model is the prediction with respect to the mass-metallicity relationship (MZR) of star-forming galaxies. This is a key result of a comprehensive spectroscopic project which revealed a tight relationship between the metallicity of the young stellar population and total galaxy stellar mass. Fig. 5 displays the latest results obtained from the analysis of individual supergiant stars (Kudritzki et al. 2024) and the stellar population synthesis studies of young stellar populations in SDSS (Sextl et al. 2023) and TYPHOON (Sextl et al. 2024) local star-forming galaxies. The Model B data point ($[Z]_{\text{NGC300}} = -0.2335$, the present-day predicted metallicity at a radius $r = 0.4R_{25}$ as for all galaxies with a metallicity gradient in this plot) fits very nicely on the relationship.

A crucial aspect of galaxy evolution is the change of the specific SFR. Figure 6 plots the time evolution of sSFR radial profiles predicted by Model B (solid line) and Model A (dashed line). The values of sSFR are high at early times, and the radial profile is nearly flat. As NGC 300 evolves, the initially flat sSFR gradient becomes steeper, due to the gas exhaustion of the inner region of the galaxy. (This trend is consistent with the model results obtained by Belfiore et al. (2019)). In addition, compared to Model A, Model B predicted sSFR values are higher during the whole evolution history of NGC 300. Radial gas inflows create higher star formation activity. Finally, the

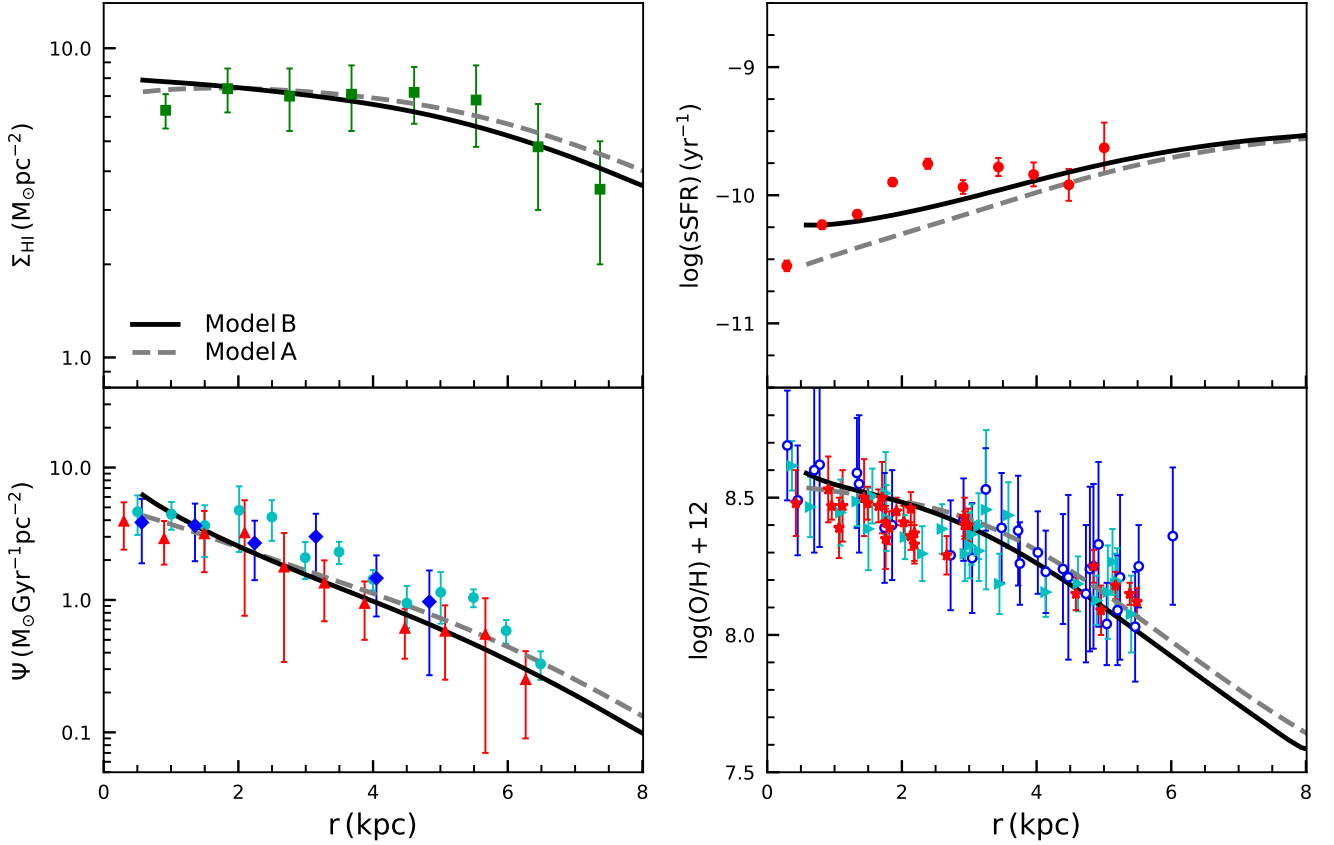


Fig. 2. Comparisons between the model predictions and the observed data of NGC 300. Solid lines correspond to the best-fitting model with a radial inflow of gas (Model B) and dashed lines to the model without radial inflow (Model A). The left-hand side shows the radial profiles of H I (top) mass and SFR (bottom) surface density, while the right-hand side displays the radial profiles of sSFR (top) and $12 + \log(\text{O}/\text{H})$ (bottom). H I data (see text) are shown by green filled squares. SFR data are separately denoted as blue filled diamonds (Gogarten et al. 2010), red filled triangles (Williams et al. 2013), and cyan filled circles Mondal et al. (2019). sSFR data (see text) are plotted by red filled cycles. $12 + \log(\text{O}/\text{H})$ data from H II regions (Bresolin et al. 2009), BSGs (Kudritzki et al. 2008), and RSGs (Gazak et al. 2015) are shown as red filled asterisks, blue open circles, and cyan filled triangles, respectively.

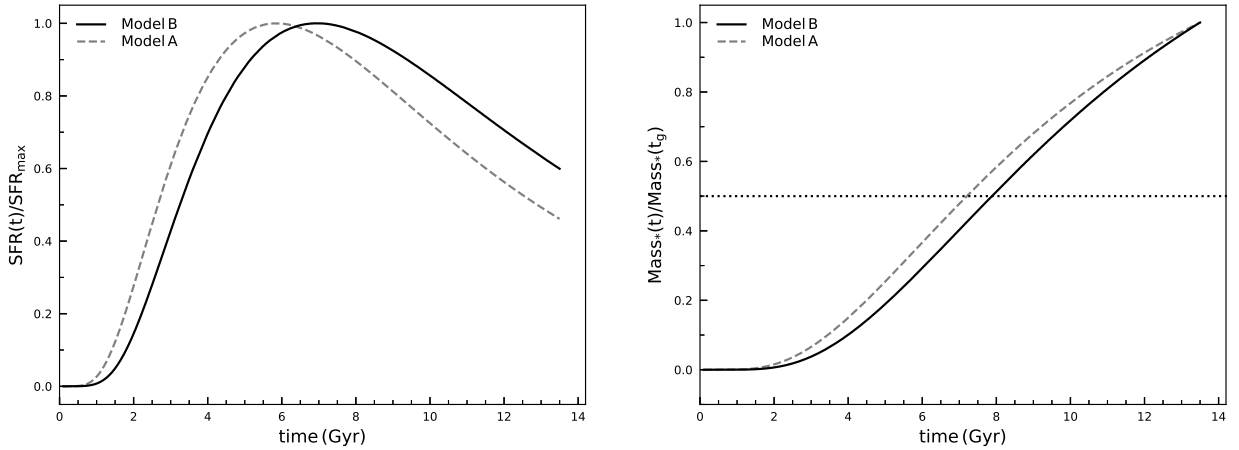


Fig. 3. SFH (left) and stellar mass growth history (right) of NGC 300 predicted by Model A (dashed line) and Model B (solid line). SFH is normalized to its maximum value, while stellar mass is normalized to its present-day value. The dotted line in the right panel denotes when the stellar mass achieves 50% of its final value.

model B predicted present-day sSFR profile (i.e., at 13.5 Gyr, black solid line) agrees well with the observed profile derived by using $(\text{FUV} - K)$ colours (Muñoz-Mateos et al. 2007). We note that the inclusion of radial gas inflows contributes to bringing the model predicted present-day sSFR profile much closer to

the observations of NGC 300 (see the right-top panel of Fig. 2), because the radial gas inflows provide more gas in the inner regions at later times.

The sSFR of NGC 300 predicted by Model B and Model A are $\log(\text{sSFR}/\text{yr}^{-1}) = -10.022$ and -10.127 , respectively. They

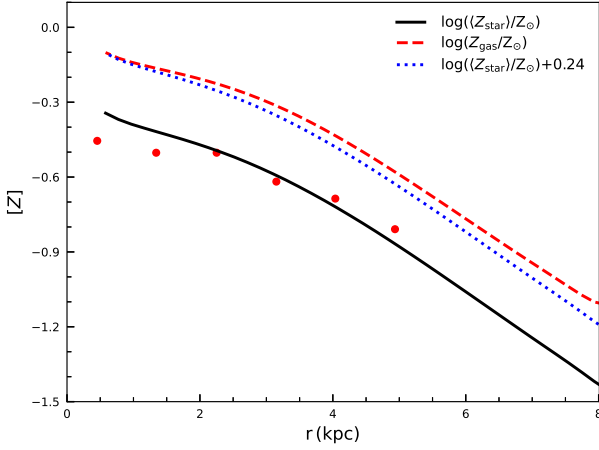


Fig. 4. Radial distribution of the mean metallicity of the entire stellar population. Observations obtained from the photometric analysis of color-magnitude diagrams (CMD, Gogarten et al. 2010) are shown as red circles and the Model B prediction is displayed as the black solid line. The Model B predicted metallicity of the ISM and the very young stars is additionally shown as the red dashed curve. For comparison purposes, the blue dotted curve represents the black curve shifted by +0.24 dex.

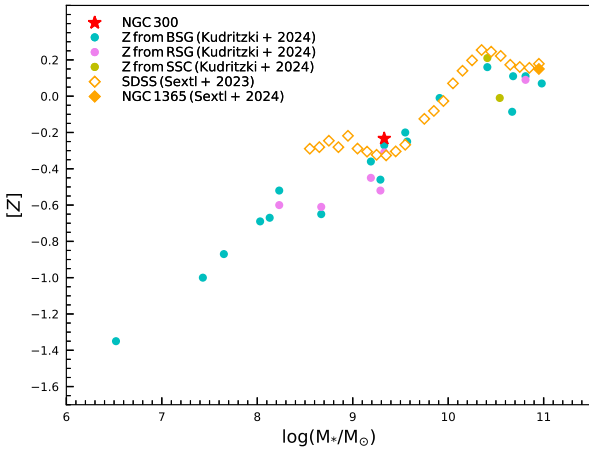


Fig. 5. The mass-metallicity relationship of star-forming galaxies. The prediction by Model B shown as a red solid star is compared with observations of a large sample of galaxies. Solid circles refer to stellar metallicity derived from spectroscopy of individual blue supergiants (cyan), red supergiants (pink), and super star clusters (yellow) (see Kudritzki et al. 2024, and references therein). The open orange diamonds represent the result of integrated galaxy spectra of young stellar population for 250,000 SDSS star-forming galaxies by using a stellar population synthesis technique (Sextl et al. 2023), while the orange solid diamonds denotes the analysis of the spatially resolved young stellar population synthesis study (Sextl et al. 2024).

agree well with the observed values (see Section 3) and fit also very nicely on the relationship with stellar mass obtained by xGASS and xCOLDGASS surveys as shown in Figure 7.

Figure 8 shows the time evolution of the radial metallicity profiles as predicted by Model B (solid line) and Model A (dashed line). The model starts at very low metallicity and with a strong metallicity gradient. Then, while the metallicity increases the gradient becomes flatter. This agrees well with one set of models and simulations (e.g., Boissier & Prantzos 2000; Mollá & Díaz 2005; Pilkington et al. 2012; Minchev et al.

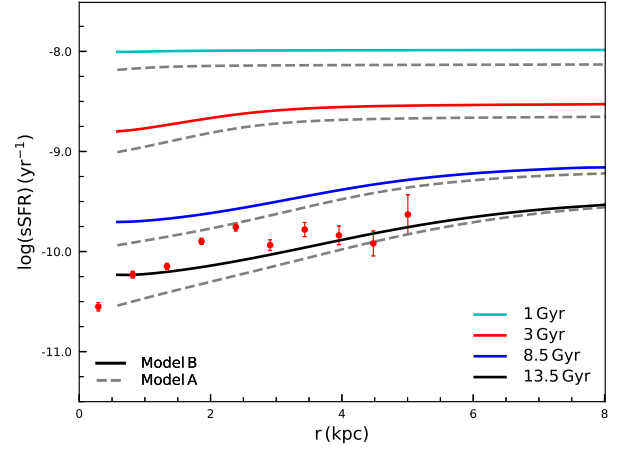


Fig. 6. Cosmic time evolution of sSFR radial profiles. Solid lines with different colours represent Model B at 1 Gyr (cyan), 3 Gyr (red), 8.5 Gyr (blue), and 13.5 Gyr (present-day, black). The corresponding results by Model A are shown as gray dashed lines. Red filled cycles are the observed data, the same as those in the right-top panel of Fig. 2.

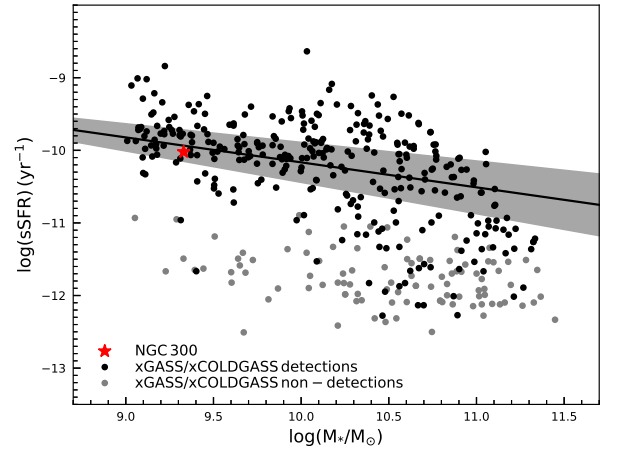


Fig. 7. Specific SFR as a function of stellar mass, both for the Model B predicted sSFR for NGC 300 (red solid star) and the observed sSFR of xGASS and xCOLDGASS (Saintonge et al. 2017; Catinella et al. 2018). The solid line refers to star-forming galaxy main sequence, and the grey shaded region represents 1σ deviation (eq. 2 in Catinella et al. 2018). Black filled circles refer to the observed SFR in nearby galaxies from xGASS and xCOLDGASS detections, while grey filled cycles denote non-detections in both xGASS and xCOLDGASS.

2018; Vincenzo & Kobayashi 2018; Acharyya et al. 2024), but is in tension with several alternative approaches (e.g., Chiappini et al. 2001; Spitoni et al. 2013; Mott et al. 2013; Schönrich & McMillan 2017; Sharda et al. 2021; Graf et al. 2024). In addition, at early times the radial gas inflows flatten the metallicity gradient, whereas at later times they steepen the gradient. This is mainly due to the fact that, at early stages of evolution, the radial gas inflows dilute the metallicity, while at later times the radial gas inflows facilitate star formation and then enrich the metallicity.

As already demonstrated by Figure 2, the present-day metallicity of the young stellar population and ISM is reproduced well by our model. Now we also add the PNe studied by Stasińska et al. (2013) (see also Magrini et al. 2016 for construction of radial bins). With an average age of the PNe progenitors of 5 Gyr, it is interesting to compare with the model metallic-

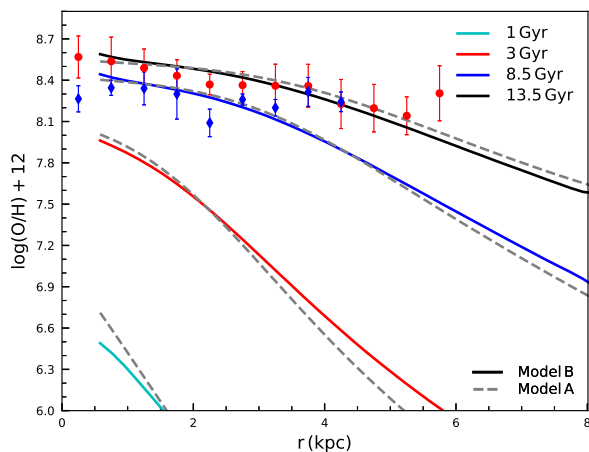


Fig. 8. Cosmic time evolution of metallicity radial profiles. Solid line with different colours represent Model B at 1 Gyr (cyan), 3 Gyr (red), 8.5 Gyr (blue), and 13.5 Gyr (present-day, black). The corresponding results predicted by Model A are shown as gray dashed lines. Red solid circles are the binned metallicity for HII regions from Bresolin et al. (2009), BSGs from Kudritzki et al. (2008), and RSGs from Gazak et al. (2015), while blue solid diamonds denote the binned metallicity of PNe from Stasińska et al. (2013).

ity at 8.5 Gyr. Except for the two outer bins, the agreement is very good. As already discussed by Stasińska et al. (2013), the oxygen abundance of these outer PNe might be affected by nucleosynthesis in the AGB PNe progenitors.

5. Conclusions

NGC 300 as a well studied isolated, bulge-less, and low-mass disc galaxy is ideally suited for an investigation of galaxy evolution. In this work, we build a bridge for NGC 300 between its observed properties and its evolution history by constructing a chemical evolution model. The main improvement of the model in this work is the inclusion of radial gas inflows. In addition, we extend the comparison and fit with the observations by adding the results of extensive non-LTE spectroscopy of very young massive stars.

Our model simultaneously reproduces the observed radial profiles of H I gas mass surface density, SFR surface density, sSFR, as well as gas-phase, young stars and mean stellar metallicity and allows us to assess the effects of radial gas flows. While the radial flow velocity is very small, ~ -0.1 km/s, it is sufficient to slightly steepen the H I gas mass and SFR surface density profile. It flattens the radial profile of sSFR significantly bringing it closer to the observations. The inclusion of radial inflows leads to increasing star formation along the disc and potentially helping to sustain star formation in local spiral arms.

The effects of radial gas inflows on the present-day radial metallicity distribution are small but the predicted influencing of the metallicity gradient when going back in time is significantly enhanced. The model predicted present-day metallicity fits nicely on the observed mass-metallicity relationship of star-forming galaxies. It also agrees with the star-forming galaxy main sequence.

Acknowledgements. We thank the anonymous referee for constructive comments and suggestions, which improved the quality of our work greatly. Xiaoyu Kang and Fenghui Zhang are supported by the Basic Science Centre project of the National Natural Science Foundation (NSF) of China (No. 12288102), the National Key R&D Program of China with (Nos. 2021YFA1600403 and

2021YFA1600400), the International Centre of Supernovae, Yunnan Key Laboratory (No. 202302AN360001), the basic research program of Yunnan Province (No. 202401AT070142). Rolf Kudritzki and Xiaoyu Kang acknowledge support by the Munich Excellence Cluster Origins and the Munich Institute for Astro-, Particle and Biophysics (MIAPbP) both funded by the Deutsche Forschungsgemeinschaft (DFG, German Research Foundation) under the German Excellence Strategy EXC-2094 390783311. Xiaoyu Kang thanks Huanian Zhang in Huazhong University of Science and Technology for helpful suggestions during revision.

References

- Acharyya, A., Peebles, M. S., Tumlinson, J., et al. 2024, arXiv:2404.06613. doi:10.48550/arXiv.2404.06613
- Asplund, M., Grevesse, N., Sauval, A. J., & Scott, P. 2009, *ARA&A*, 47, 481
- Belfiore, F., Vincenzo, F., Maiolino, R., et al. 2019, *MNRAS*, 487, 456.
- Binder, B., Williams, B. F., Eracleous, M., et al. 2012, *ApJ*, 758, 15. doi:10.1088/0004-637X/758/1/15
- Binder, B. A., Williams, R., Payne, J., et al. 2024, *ApJ*, 969, 97. doi:10.3847/1538-4357/ad46d9
- Bird, J. C., Kazantzidis, S., & Weinberg, D. H. 2012, *MNRAS*, 420, 913. doi:10.1111/j.1365-2966.2011.19728.x
- Bland-Hawthorn, J., Vlahić, M., Freeman, K. C., et al. 2005, *ApJ*, 629, 239. doi:10.1086/430512
- Boissier, S. & Prantzos, N. 2000, *MNRAS*, 312, 398
- Bresolin, F., Gieren, W., Kudritzki, R.-P., et al. 2009, *ApJ*, 700, 309
- Bresolin, F., Kudritzki, R.-P., & Urbaneja, M. A. 2022, *ApJ*, 940, 32
- Calura, F., Palla, M., Morselli, L., et al. 2023, *MNRAS*, 523, 2351. doi:10.1093/mnras/stad1316
- Carr, C., Johnston, K. V., Laporte, C. F. P., et al. 2022, *MNRAS*, 516, 5067. doi:10.1093/mnras/stac2403
- Casasola, V., Cassarà, L. P., Bianchi, S., et al. 2017, *A&A*, 605, A18
- Casasola, V., Bianchi, S., Magrini, L., et al. 2022, *A&A*, 668, A130. doi:10.1051/0004-6361/202245043
- Catinella, B., Saintonge, A., Janowiecki, S., et al. 2018, *MNRAS*, 476, 875. doi:10.1093/mnras/sty089
- Chang, R. X., Hou, J. L., Shen, S. Y., & Shu, C. G. 2010, *ApJ*, 722, 380
- Chen, Q.-H., Grasha, K., Battisti, A. J., et al. 2023, *MNRAS*, 519, 4801
- Chiappini, C., Matteucci, F., & Romano, D. 2001, *ApJ*, 554, 1044
- Cohen, R. E., McQuinn, K. B. W., Murray, C. E., et al. 2024, *ApJ*, 975, 42.
- Dalcanton, J. J., Yoachim, P., & Bernstein, R. A. 2004, *ApJ*, 608, 189. doi:10.1086/386358
- Dalcanton, J. J., Williams, B. F., Seth, A. C., et al. 2009, *ApJS*, 183, 67
- Daniel, K. J. & Wyse, R. F. G. 2015, *MNRAS*, 447, 3576. doi:10.1093/mnras/stu2683
- Davies, B., Kudritzki, R. P., Lardo, C. et al. *ApJ*, 847, 112
- Di Teodoro, E. M. & Peek, J. E. G. 2021, *ApJ*, 923, 220. doi:10.3847/1538-4357/ac2cbd
- Edvardsson, B., Andersen, J., Gustafsson, B., et al. 1993, *A&A*, 500, 391
- Erb, D. K. 2008, *ApJ*, 674, 151
- Feillet, D. K., Frankel, N., Lind, K., et al. 2019, *MNRAS*, 489, 1742
- Finlator, K. & Davé, R. 2008, *MNRAS*, 385, 2181
- Frankel, N., Sanders, J., Rix, H.-W., et al. 2019, *ApJ*, 884, 99
- Fraser-McKelvie, A., Cortese, L., Groves, B., et al. 2022, *MNRAS*, 510, 320. doi:10.1093/mnras/stab3430
- Gazak, J. Z., Kudritzki, R., Evans, C., et al. 2015, *ApJ*, 805, 182
- Gieren, W., Pietrzyński, G., Soszyński, I., et al. 2005, *ApJ*, 628, 703
- Graf, R. L., Wetzel, A., Bailin, J., et al. 2024, arXiv:2410.21377. doi:10.48550/arXiv.2410.21377
- Gogarten, S. M., Dalcanton, J. J., Williams, B. F., et al. 2010, *ApJ*, 712, 858
- Goswami, S., Slemer, A., Marigo, P., et al. 2021, *A&A*, 650, A203
- Grisoni, V., Spitoni, E., & Matteucci, F. 2018, *MNRAS*, 481, 2570
- Halliday, C., Daddi, E., Cimatti, A., et al. 2008, *A&A*, 479, 417.
- Haywood, M. 2008, *MNRAS*, 388, 1175
- Haywood, M., Snaith, O., Lehnert, M. D., et al. 2019, *A&A*, 625, A105. doi:10.1051/0004-6361/201834155
- Halle, A., Di Matteo, P., Haywood, M., et al. 2015, *A&A*, 578, A58. doi:10.1051/0004-6361/201525612
- Helou, G., Roussel, H., Appleton, P., et al. 2004, *ApJS*, 154, 253. doi:10.1086/422640
- Hirschmann, M., De Lucia, G., & Fontanot, F. 2016, *MNRAS*, 461, 1760
- Ho, I.-T., Kudritzki, R.-P., Kewley, L. J., et al. 2015, *MNRAS*, 448, 2030
- Izotov, Y. I., Stasińska, G., Meynet, G., et al. 2006, *A&A*, 448, 955
- Kang, X., Zhang, F., Chang, R., Wang, L., & Cheng, L. 2016, *A&A*, 585, A20
- Kang, X., Chang, R., Kudritzki, R.-P., et al. 2021, *MNRAS*, 502, 1967
- Kang, X., Kudritzki, R.-P., & Zhang, F. 2023, *A&A*, 679, A83
- Karachentsev, I. D., Grebel, E. K., Sharina, M. E., et al. 2003, *A&A*, 404, 93. doi:10.1051/0004-6361:20030170

- Karachentsev, I. D. & Kaisina, E. I. 2013, *AJ*, 146, 46. doi:10.1088/0004-6256/146/3/46
- Kauffmann, G., White, S. D. M., & Guiderdoni, B. 1993, *MNRAS*, 264, 201. doi:10.1093/mnras/264.1.201
- Robotham, A. S. G., et al. 2014, *MNRAS*, 444, 1647
- Khoperskov, S., Di Matteo, P., Haywood, M., et al. 2020, *A&A*, 638, A144. doi:10.1051/0004-6361/201937188
- Kroupa, P., Tout, C. A., & Gilmore, G. 1993, *MNRAS*, 262, 545
- Kruijssen, J. M. D., Schruha, A., Cheance, M., et al. 2019, *Nature*, 569, 519. doi:10.1038/s41586-019-1194-3
- Krumholz, M. R. 2014, *Phys. Rep.*, 539, 49.
- Kubryk, M., Prantzos, N., & Athanassoula, E. 2013, *MNRAS*, 436, 1479
- Kubryk, M., Prantzos, N., & Athanassoula, E. 2015, *A&A*, 580, A126
- Kudritzki, R.-P., Urbaneja, M. A., Bresolin, F., et al. 2008, *ApJ*, 681, 269
- Kudritzki, R.-P., Ho, I.-T., Schruha, A., et al. 2015, *MNRAS*, 450, 342
- Kudritzki, R.-P., Teklu, A. F., Schulze, F., et al. 2021, *ApJ*, 910, 87
- Kudritzki, R.-P., Urbaneja, M. A., Bresolin, F., et al. 2024, *ApJ*, 977, 217. doi:10.3847/1538-4357/ad9279
- Lacey, C. G. & Fall, S. M. 1985, *ApJ*, 290, 154.
- Larson, R. B. 1972, *Nature*, 236, 21. doi:10.1038/236021a0
- Larson, R. B. 1974, *MNRAS*, 169, 229. doi:10.1093/mnras/169.2.229
- Larson, R. B. 1976, *MNRAS*, 176, 31
- Leroy, A. K., Walter, F., Brinks, E., et al. 2008, *AJ*, 136, 2782
- Lian, J., Thomas, D., & Maraston, C. 2018a, *MNRAS*, 481, 4000
- Lian, J., Thomas, D., Maraston, C., et al. 2018b, *MNRAS*, 476, 3883
- Lian, J., Zasowski, G., Hasselquist, S., et al. 2022, *MNRAS*, 511, 5639. doi:10.1093/mnras/stac479
- Liu, C., Kudritzki, R.-P., Zhao, G., et al. 2022, *ApJ*, 932, 29
- Loebman, S. R., Debatista, V. P., Nidever, D. L., et al. 2016, *ApJ*, 818, L6. doi:10.3847/2041-8205/818/1/L6
- Maciel, W. J., Costa, R. D. D., & Uchida, M. M. M. 2003, *A&A*, 397, 667
- Magrini, L., Stanghellini, L., & Villaver, E. 2009, *ApJ*, 696, 729
- Magrini, L., Coccato, L., Stanghellini, L., et al. 2016, *A&A*, 588, A91
- Maiolino, R. & Mannucci, F. 2019, *A&A Rev.*, 27, 3. doi:10.1007/s00159-018-0112-2
- Matteucci, F. & Francois, P. 1989, *MNRAS*, 239, 885
- Matteucci, F. 2021, *A&A Rev.*, 29, 5. doi:10.1007/s00159-021-00133-8
- Mayor, M. & Vigroux, L. 1981, *A&A*, 98, 1
- Minchev, I. & Famaey, B. 2010, *ApJ*, 722, 112
- Minchev, I., Anders, F., Recio-Blanco, A., et al. 2018, *MNRAS*, 481, 1645. doi:10.1093/mnras/sty2033
- Mollá, M. & Díaz, A. I. 2005, *MNRAS*, 358, 521
- Mondal, C., Subramaniam, A., & George, K. 2019, *Journal of Astrophysics and Astronomy*, 40, 35.
- Mott, A., Spitoni, E., & Matteucci, F. 2013, *MNRAS*, 435, 2918. doi:10.1093/mnras/stt1495
- Moustakas, J., Kennicutt, R. C., Tremonti, C. A., et al. 2010, *ApJS*, 190, 233
- Muñoz-Mateos, J. C., Gil de Paz, A., Boissier, S., et al. 2007, *ApJ*, 658, 1006
- Nantais, J. B., Huchra, J. P., Barmby, P., et al. 2010, *AJ*, 139, 1178. doi:10.1088/0004-6256/139/3/1178
- Olsen, K. A. G., Miller, B. W., Suntzeff, N. B., et al. 2004, *AJ*, 127, 2674. doi:10.1086/383297
- Pagel, B. E. J. 1997, *Nucleosynthesis and Chemical Evolution of Galaxies*, by Bernard E. J. Pagel, pp. 392. ISBN 0521550610. Cambridge, UK: Cambridge University Press, October 1997., 392
- Peng, Y.-jie . & Maiolino, R. 2014, *MNRAS*, 443, 3643.
- Pilkington, K., Few, C. G., Gibson, B. K., et al. 2012, *A&A*, 540, A56. doi:10.1051/0004-6361/201117466
- Pilyugin, L. S., Grebel, E. K., & Kniazev, A. Y. 2014, *AJ*, 147, 131
- Pipino, A., Lilly, S. J., & Carollo, C. M. 2014, *MNRAS*, 441, 1444.
- Pointon, S. K., Kacprzak, G. G., Nielsen, N. M., et al. 2019, *ApJ*, Relationship between the Metallicity of the Circumgalactic Medium and Galaxy Orientation, 883, 1, 78. doi:10.3847/1538-4357/ab3b0e
- Portinari, L. & Chiosi, C. 2000, *A&A*, 355, 929. doi:10.48550/arXiv.astro-ph/0002145
- Prantzos, N. & Boissier, S. 2000, *MNRAS*, 313, 338
- Prochaska, J. X., Werk, J. K., Worseck, G., et al. 2017, *ApJ*, The COS-Halos Survey: Metallicities in the Low-redshift Circumgalactic Medium, 837, 2, 169. doi:10.3847/1538-4357/aa6007
- Quillen, A. C., Minchev, I., Bland-Hawthorn, J., et al. 2009, *MNRAS*, 397, 1599. doi:10.1111/j.1365-2966.2009.15054.x
- Recchi, S., Spitoni, E., Matteucci, F., et al. 2008, *A&A*, 489, 555
- Rogers, N. S. J., Skillman, E. D., Pogge, R. W., et al. 2022, *ApJ*, 939, 44
- Romano, D., Karakas, A. I., Tosi, M., et al. 2010, *A&A*, 522, A32
- Roškar, R., Debatista, V. P., Stinson, G. S., et al. 2008, *ApJ*, 675, L65
- Saintonge, A., Catinella, B., Tacconi, L. J., et al. 2017, *ApJS*, 233, 22. doi:10.3847/1538-4365/aa97e0
- Sánchez Almeida, J., Elmegreen, B. G., Muñoz-Tuñón, C., et al. 2014, *A&A Rev.*, 22, 71
- Sánchez-Blázquez, P. 2020, *IAU General Assembly*, 261. doi:10.1017/S1743921319004277
- Schmidt, M. 1963, *ApJ*, 137, 758
- Schönrich, R. & Binney, J. 2009, *MNRAS*, 396, 203
- Schönrich, R. & McMillan, P. J. 2017, *MNRAS*, 467, 1154
- Sellwood, J. A. & Binney, J. J. 2002, *MNRAS*, 336, 785. doi:10.1046/j.1365-8711.2002.05806.x
- Sextl, E., Kudritzki, R.-P., Weller, J., et al. 2021, *ApJ*, 914, 94
- Sextl, E., Kudritzki, R.-P., Zahid, H. J., et al. 2023, *ApJ*, 949, 60
- Sextl, E., Kudritzki, R.-P., Burkert, A., et al. 2024, *ApJ*, 960, 83.
- Sharda, P., Krumholz, M. R., Wisnioski, E., et al. 2021, *MNRAS*, 502, 5935
- Spitoni, E. & Matteucci, F. 2011, *A&A*, 531, A72. doi:10.1051/0004-6361/201015749
- Spitoni, E., Matteucci, F., & Marcon-Uchida, M. M. 2013, *A&A*, 551, A123
- Spitoni, E., Romano, D., Matteucci, F., et al. 2015, *ApJ*, 802, 129
- Spitoni, E., Vincenzo, F., & Matteucci, F. 2017, *A&A*, 599, A6
- Spitoni, E., Giovannini, L., & Matteucci, F. 2017, *A&A*, 605, A38. doi:10.1051/0004-6361/201730545
- Spitoni, E., Cescutti, G., Minchev, I., et al. 2019, *A&A*, 628, A38
- Spitoni, E., Calura, F., Mignoli, M., et al. 2020, *A&A*, 642, A113
- Spitoni, E., Verma, K., Silva Aguirre, V., et al. 2021a, *A&A*, 647, A73
- Spitoni, E., Calura, F., Silva Aguirre, V., et al. 2021b, *A&A*, 648, L5
- Stanghellini, L., Magrini, L., Casasola, V., et al. 2014, *A&A*, 567, A88
- Stasińska, G., Peña, M., Bresolin, F., et al. 2013, *A&A*, 552, A12
- Thon, R. & Meusinger, H. 1998, *A&A*, 338, 413
- Tinsley, B. M. & Larson, R. B. 1978, *ApJ*, 221, 554.
- Toribio San Cipriano, L., García-Rojas, J., Esteban, C., et al. 2016, *MNRAS*, 458, 1866. doi:10.1093/mnras/stw397
- Tremonti, C. A., Heckman, T. M., Kauffmann, G., et al. 2004, *ApJ*, 613, 898
- van den Bergh, S. 1962, *AJ*, 67, 486
- Vincenzo, F., Matteucci, F., Belfiore, F., et al. 2016, *MNRAS*, 455, 4183
- Vincenzo, F. & Kobayashi, C. 2018, *MNRAS*, 478, 155. doi:10.1093/mnras/sty1047
- Vincenzo, F. & Kobayashi, C. 2020, *MNRAS*, 496, 80
- Vlajić, M., Bland-Hawthorn, J., & Freeman, K. C. 2009, *ApJ*, 697, 361. doi:10.1088/0004-637X/697/1/361
- Westmeier, T., Braun, R., & Koribalski, B. S. 2011, *MNRAS*, 410, 2217.
- Williams, B. F., Dalcanton, J. J., Stilp, A., et al. 2013, *ApJ*, 765, 120
- Xiang, M. & Rix, H.-W. 2022, *Nature*, 603, 599
- Yin, J., Hou, J. L., Prantzos, N., et al. 2009, *A&A*, 505, 497
- Yin, J., Shen, S., & Hao, L. 2023, *ApJ*, 958, 34. doi:10.3847/1538-4357/acfa6b
- Zaritsky, D., Kennicutt, R. C., & Huchra, J. P. 1994, *ApJ*, 420, 87
- Zinchenko, I. A., Just, A., Pilyugin, L. S., et al. 2019, *A&A*, 623, A7. doi:10.1051/0004-6361/201834364